

Accepted Manuscript

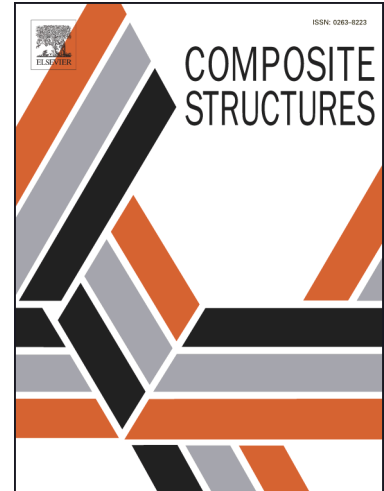
Modeling for CFRP structures subjected to quasi-static crushing

Guohua Zhu, Guangyong Sun, Guangyao Li, Aiguo Cheng, Qing Li

PII: S0263-8223(17)30885-1
DOI: <http://dx.doi.org/10.1016/j.compstruct.2017.09.001>
Reference: COST 8864

To appear in: *Composite Structures*

Received Date: 18 March 2017
Revised Date: 20 July 2017
Accepted Date: 12 September 2017



Please cite this article as: Zhu, G., Sun, G., Li, G., Cheng, A., Li, Q., Modeling for CFRP structures subjected to quasi-static crushing, *Composite Structures* (2017), doi: <http://dx.doi.org/10.1016/j.compstruct.2017.09.001>

This is a PDF file of an unedited manuscript that has been accepted for publication. As a service to our customers we are providing this early version of the manuscript. The manuscript will undergo copyediting, typesetting, and review of the resulting proof before it is published in its final form. Please note that during the production process errors may be discovered which could affect the content, and all legal disclaimers that apply to the journal pertain.

Modeling for CFRP structures subjected to quasi-static crushingGuohua Zhu¹, Guangyong Sun^{1,2,*}, Guangyao Li¹, Aiguo Cheng¹, Qing Li²¹State Key Laboratory of Advanced Design and Manufacture for Vehicle Body,

Hunan University, Changsha, 410082, China

²School of Aerospace, Mechanical and Mechatronic Engineering, The University of

Sydney, Sydney, NSW 2006, Australia

Abstract

Carbon fiber reinforced plastic (CFRP) composite materials demonstrate significant promise to further improve weight to performance in automotive engineering. Nevertheless, design of CFRP components for crashworthiness criteria remains rather challenging and typically requires laborious trial-and-error processes. This study aims to promote computational design of CFRP structures by establishing effective constitutive model that is implemented in the commercial finite element code Abaqus/Explicit. Two different numerical models (namely, the single layer shell model and the stacked shell model) were developed to simulate experimental crushing tests on the square CFRP tube. The effects of key parameters for these two FE models were analyzed, respectively. The comparisons of numerical results with experimental data indicated that the 9 layers stacked shell model is capable of reproducing experimental results with relatively high accuracy. Based on the validated modeling approach, crushing behaviors of several CFRP thin-walled structures with different cross sectional geometries and thicknesses were further explored. The failure modes and key indicators in relation to the structural crashworthiness were investigated for identifying a best possible sectional configuration. It is found that the circular tube shows superior specific energy absorption capacity of all different tubal configurations with the same wall thickness, meaning that the tube with circular section is of good potential as a crashworthy CFRP structure.

Keywords: Crashworthiness, Energy absorption, CFRP tubes, Failure mechanism, Constitutive model.

* Corresponding Author: Tel: +86-13786196408; Fax: +86-(0)73188822051; Email: sgy800@126.com

1. Introduction

Over the past decades, composite materials have been gradually used in industry sectors ranging from aerospace to automobile [1-5]. Compared with the traditional metallic materials, composites exhibited higher specific strength and specific energy absorption capacity to the weight, which provides great opportunity to save vehicular weight and enhance structural performance [6-8].

Recently, carbon fibers reinforced plastics (CFRP), as one class of typical composite materials, have been introduced in vehicular engineering for improving fuel economy and structural safety [9-14]. There have been substantial studies on crashworthiness of various CFRP structures in literature. For example, Mahdi et al. [15] conducted experimental studies on the effect of fiber orientation on the energy absorption characteristics of composite tubes subjected to axial loading. They showed the certain advantages of laying fiber orientations of $15^\circ/-75^\circ$ and $75^\circ/-15^\circ$ for enhancing the load carrying capacity and energy absorption. Israr et al. [16] carried out the quasi-static tests on different configurations of unidirectional fiber and woven fiber composites to investigate the crushing behaviors of one ply under crushing load. Mamalis et al. [6] explored the crushing characteristics of thin-walled square CFRP tubes under static and dynamic axial compressive loads, experimentally; and they found that crushing behaviors of square CFRP tubes are fairly brittle due to the characteristics of the constituent materials. From the previous studies reported in literature, it can be concluded that the crushing behaviors of CFRP structures are generally determined by development of fracture, inter-ply delamination and extensive micro-cracking, which depend on structural and material features, such as fiber orientation, number of stacking layers, properties of each single layer, etc. These factors make the design of CFRP energy-absorbing structures much more sophisticated and challenging than traditional metallic structures.

Typically, the development of crashworthy structures largely relies upon laborious and costly experimental tests. With the fast advances in computational techniques, the ability of numerical simulations for accurately predicting the crushing behaviors has improved remarkably, thereby reducing the development cycle and cost of composite components [17-20]. As the most representative methods, the finite element (FE) simulations have played a very important role in the early phase of the crashworthiness design. For metal based

energy-absorbing structures, the FE models have been capable to generate excellent prediction thanks to well-established constitutive behaviors [18, 21]. For modeling of CFRP structures, it is essential to reproduce the complex crushing behaviors precisely by establishing more complex constitutive models. There have been different modeling approaches to study the numerical simulation for CFRP structures in literature to date. The first is to develop a micro-mechanical model that simulates the details on the level of fiber/matrix interactions with a focus on fracture analysis and crack growth simulation [22-24]. However, such models could be too expensive to analyze large components with complex microstructures. The second is macro-mechanical model that provides a macroscopic description of the bulk structural behaviors for CFRP. In the macro-mechanical model, the micro-mechanical materials are simplified into the homogeneous anisotropic medium. Currently, it seems that the macro-mechanical model is more extensively used for engineering design of CFRP structure attributable to its high computational efficiency. It is noted that Chiu et al. [25] detailed the theory and implementation of a composite damage model based on macro-mechanical 3D model, addressing intralaminar and interlaminar failure behaviors, for the crushing simulation of unidirectional composite tubes; which showed good agreement with the experimental results [25]. Alternatively, our presented study here aimed to develop a macro-mechanical shell model for simulating crushing behaviors of woven fabric composites, which have different constitutive model of unidirectional composites. This is mainly because most of vehicle body components are made in thin-walled components and experimental tests of out-of-plane behaviors of CFRP can be complex and time-consuming [9, 26].

The macro-mechanical shell model can be classified into the single shell layer model and the stacked shell model. The single shell layer model employs a single layer of shell elements to model the structure. Although it cannot be used to properly predict the inter-laminar failure occurred in laminated CFRP subjected to crushing loads, it makes certain sense if only the predictions of overall loading capacity and energy absorption are required. Note that there have been substantial studies on crushing behaviors of various CFRP structures through the single shell layer models. For example, Luo et al. [27] developed a stiffness degraded model by incorporating the extended Hashin failure criterion and damage evolution law from the continuum damage mechanics, to predict progressive failure of CFRP tubes under axial

dynamic impact. Their simulation results showed that the proposed single layer shell model can be applied to estimate the energy-absorbing characteristics of CFRP tubes. Boria et al. [28] used the single layer shell elements to investigate the impact behaviour of composite front crash structures. Liu et al. [9] employed the single layer shell model to investigate the structural crashworthiness of CFRP electric vehicle body under the roof crash and pole side impact, respectively. Bussadori et al. [29] numerically investigated crashworthiness characteristics of a CFRP tube by using single shell layer models, and the results demonstrated the advantages of this modeling approach. It can be concluded from these exemplified studies that the single shell layer modeling approach is suitable for engineering applications thanks to its modeling simplicity and computational effectiveness. However, it may be not capable to capture some detailed failure modes observed in the experimental tests.

The stacked shell modeling approach, on the other hand, comprises of more than one layer of shell elements by joining them together using specific elements (such as cohesive elements etc.) which allows modeling the CFRP structures more realistically. Such a model is capable to simulate the inter-laminar failure due to the presence of the joining elements between the layers. Not only does it provide better physical representation of the complex failure modes, but also keeps the simplicity inherent of the macro-mechanical approach. In this regard, for example, Sokolinsky et al. [30] presented a stacked shell model of a corrugated CFRP plate subjected to quasi-static crushing, and the numerical results showed very good quantitative and qualitative agreement with the experimental data. Xiao et al. [31] examined the application of a composite damage model (i.e. MAT 58 in LS-DYNA) for crush simulations of braided composite tube by adopting the stacked shell modeling. Joosten et al. [7] described the quasi-static crushing behaviors of CFRP hat-shaped crush components by using a four-layer stacked shell model. The numerical result indicated that this modeling approach is capable to predict the failure modes more accurately and provide better agreement with the load-displacement curves generated from the experiments. In other words, the stacked shell modeling approach can better capture the failure details with a relatively simple constitutive relation for numerical simulation of CFRP structures.

In review of aforementioned studies in literature, it is known that the macro-mechanical model is more applicable for engineering crashing analysis of CFRP structure attributable to

its high computational efficiency. In this study, two different macro-mechanical modeling approaches, namely the single layer shell modeling and the stacked shell modeling, were adopted to investigate the axial crushing behaviors of square CFRP tubes. The effects of key parameters were examined using these two modeling approaches respectively. By comparing the numerical results with the experimental data, the overall suitability of these two models was assessed for providing a better prediction accuracy. Further, based on the suitable modeling approach, crushing behaviors of several CFRP thin-walled candidate structures with different cross sectional shapes and wall thickness were then explored. The effect of several key parameters on failure modes and crushing behaviors were investigated in these configurations, thereby providing technical guide for enhancing the crushing performance of CFRP thin-walled structures.

2. Experimental methods

2.1 Crashworthiness metrics

The general goal of designing a crashworthy structure is to reduce occupant injury by absorbing as much impact energy as possible and lowering the peak impact loads [32, 33]. The energy absorption during the crushing can be mathematically calculated as:

$$EA = \int_0^d F(x) dx, \quad (1)$$

where EA is energy absorption; d denotes crushing distance and $F(x)$ represents crushing force.

To evaluate weight efficiency of energy absorption of a structure, the specific energy absorption (SEA) is often used as:

$$SEA = \frac{EA}{m}, \quad (2)$$

where m is the mass of the crash structure. A higher SEA indicates a higher energy-absorbing efficiency of the structure.

The peak crushing force (PCF) means the maximum impact load during the crushing process, which is often associated with deceleration in dynamic crushing. The crush force efficiency (CFE) indicates the ratio of the mean crushing force (F_{mean}) to the PCF , defined as:

$$CFE = \frac{F_{mean}}{PCF} \quad (3)$$

CFE should be as high as possible to balance the peak force and energy absorption efficiency.

2.2 Experimental specimens

Three thin-walled square CFRP tubes were considered in the experimental study here. The tubes were fabricated in the woven fabric carbon–epoxy prepreg produced by Toray industries through the bladder molding process [34–36], which basically consisted of cutting prepreps, winding on mandrel, taking out the mandrel, placing into a metal mold, exerting pressure inside from an inflatable bladder, and curing within a hot press. All specimen have 1.98 mm in thickness (9 plies) with a stacking sequence of $(0^\circ, 90^\circ)_9$, 50 mm in length and 60 mm in outer side length. The two different chamfers were also considered in T-2 and T-3, as shown in Fig. 1.

Fig. 1 (a) The CFRP tube without chamfer (T-1); (b) The CFRP tube with single-sided chamfer (T-2); (c) The CFRP tube with bar chamfer (T-3).

2.3 Material characterization

In order to develop effective numerical models, a series of tensile tests was conducted to obtain the mechanical properties of the CFRP tube. The specimens were cut from the plate made of the same materials with the tube, in particular along 0° and 90° for the tensile tests, and along 45° for the in-plane shear tests (Fig. 2(a) and (b)). The tensile and in-plane shear tests were carried out according to the ASTM D3039 and D3518 procedures, respectively. The strain of the specimens was measured by digital image correlation (DIC) test system, as shown in Fig. 4(d). The typical stress–strain curves are illustrated in Fig. 3.

Fig. 2 Specimens for tensile tests and shear test: (a) The specimen and fiber orientations for tensile test; (b) The specimen and fiber orientations for shear test; (c) The specimen with CFRP tabs and speckle for DIC; (d) The specimen in the testing machine and set-up of DIC system.

Fig. 3 Typical stress–strain curves of CFRP materials: (a) Tensile tests; (b) Shear tests.

2.4 Quasi-static test

The CFRP tubes were tested in compression between two flat steel platens in a standard universal testing machine INSTRON-5985 with a load capacity of 150 kN. The test was performed in a quasi-static condition with a constant loading rate of 4 mm/min at the room temperature throughout the test. The final crushing displacement for axial compression test was set to be 35 mm (i.e. 70% of the overall specimen's height). The deformation details were photographed during the entire quasi-static loading process, and the force and displacement data were recorded.

2.5 Experimental results

The typical force–displacement curves and some snapshots of deformation modes for all specimens at the several representative positions are provided in Fig. 4. The region before reaching the initial peak force is named as the pre-crushing stage, where the force–displacement relationship is almost linear and an elastic deformation of the tube is observed. The region after the initial peak load is known as the post-crushing stage. In light of the curves, there is little difference between these three different tubes during the post-crushing stage. This is mainly because all the specimens were crushed in a fairly similar fashion during the post-crushing stage, where progressive crushing of the tube was initiated at the incident (top) end with propagation of the intra/interlaminar cracks and the cracks split the tube into external and internal fronds. As tubal compression progressed, four small external fronds were observed at the corners of the tube as a result of fiber failure. Meanwhile, the outward fronds were extensively bent and curled downwards, resulting in a series of fluctuations of crushing force around the mean crush load. A similar final deformation mode can be observed in all the specimens as shown in Fig. 5, indicating little influence of chamfer on deformation mode of the tubes. Additionally, it is worth noting that the initial peak forces with chamfer were much less than that without chamfer, and specimen T-3 showed a relatively low load carrying capacity in the early stage of compression process due to the presence of bar chamfer. Crashworthiness indicators obtained from the force and

displacement data are summarized in Table 1.

Fig. 4 (a) Typical force–displacement curves; (b) Crushing history in the axial crushing tests.

Fig. 5 All specimens after compressive test: (a) T-1; (b) T-2; (c) T-3.

Table 1 Crashworthiness indicators obtained from the crushing experimental tests.

3. Numerical modeling

3.1 Constitutive model

The FE models were developed using commercial FE software ABAQUS/Explicit. As abovementioned, two FE models (i.e. single layer shell model and stacked shell model) were created. The constitutive behavior of the single layer shell model was based upon the constitutive law for intra-laminar failure model. In the stacked shell model, the delamination failure modes were included, and consequently its constitutive behavior was based upon two individual constitutive laws for intra-laminar failure mode and inter-laminar failure mode.

The intra-laminar failure mechanism was related to the fiber damage and matrix cracking, while the inter-laminar failure mechanism was associated with the delamination failure between the layers. The constitutive models applied for modeling the intra-laminar and inter-laminar failure mechanisms were outlined as follows.

3.1.1 Intra-laminar failure

The intra-laminar failure model was implemented by utilizing a user-defined material subroutine VUMAT. The fiber damage under tensile or compressive loading and plastic deformation under shear loading were involved. The model was governed by several material properties and coefficients; and for completeness of the paper, a summary of the intra-laminar failure model is given here.

The plain woven fabric reinforcement considered in the present material constitutive model was assumed to have orthogonal fiber (tow) directions; and the intra-laminar stress–strain relation is defined as [30],

$$\begin{Bmatrix} \varepsilon_{11} \\ \varepsilon_{22} \\ \varepsilon_{12}^{el} \end{Bmatrix} = \begin{bmatrix} \frac{1}{(1-d_1)E_1} & \frac{-\nu_{12}}{E_1} & 0 \\ \frac{-\nu_{21}}{E_2} & \frac{1}{(1-d_2)E_2} & 0 \\ 0 & 0 & \frac{1}{(1-d_{12})2G_{12}} \end{bmatrix} \begin{Bmatrix} \sigma_{11} \\ \sigma_{22} \\ \sigma_{12} \end{Bmatrix} \quad (4)$$

where subscripts 1 and 2 represent fiber directions (1 for longitudinal direction and 2 for transversal direction); $\sigma = \{\sigma_{11} \ \sigma_{22} \ \sigma_{12}\}^T$ is the stress vector; $\varepsilon = \{\varepsilon_{11} \ \varepsilon_{22} \ \varepsilon_{12}^{el}\}^T$ is the elastic strain vector; E_1 and E_2 are the Young's moduli in the longitudinal and transversal directions respectively; ν_{12} is the in-plane Poisson ratio, and G_{12} is the in-plane shear modulus. d_1 and d_2 represent the damage variables related to fiber fracture in the longitudinal and transversal directions respectively; d_{12} is the damage variable associated with the matrix micro-cracking under shear loading. The damage variables, d_1 and d_2 , are further distinguished as d_{1+} , d_{1-} , d_{2+} , and d_{2-} , according to the stress state in the corresponding direction (subscripts + and - represent tensile and compressive states, respectively).

The initiation and evolution of the individual damage mechanisms were described by means of the corresponding effective stress $\hat{\sigma}$ [30], as ($i=1, 2$):

$$\hat{\sigma}_{i+} = \frac{\langle \sigma_{ii} \rangle}{1-d_{i+}} \quad \hat{\sigma}_{i-} = \frac{\langle -\sigma_{ii} \rangle}{1-d_{i-}} \quad \hat{\sigma}_{12} = \frac{\sigma_{12}}{1-d_{12}} \quad (5)$$

where angle brackets $\langle \rangle$ represent the Macaulay operator.

Considering characteristics of the woven fabric reinforcement, the mechanical properties of longitudinal and transversal directions should be almost consistent. Based on that, the failure criteria which include five different failure modes can be defined as follows:

Fiber tensile damage in longitudinal direction:

$$F_{1+} = \frac{\hat{\sigma}_{11}}{X_{1+}} \quad (6)$$

Fiber compression damage in longitudinal direction:

$$F_{1-} = -\frac{\hat{\sigma}_{11}}{X_{1-}} \quad (7)$$

Fiber tensile damage in transversal direction:

$$F_{2+} = \frac{\hat{\sigma}_{22}}{X_{2+}} \quad (8)$$

Fiber compression damage in transversal direction:

$$F_{2-} = -\frac{\hat{\sigma}_{22}}{X_{2-}} \quad (9)$$

In-plane shearing:

$$F_{12} = \left| \frac{\hat{\sigma}_{12}}{S} \right| \quad (10)$$

where X_{1+} and X_{1-} are the tensile and compressive strengths in the longitudinal direction; X_{2+} and X_{2-} are the tensile and compressive strengths in the transversal direction; S is in-plane shear strength. F_{1+} , F_{1-} , F_{2+} , F_{2-} and F_{12} are the failure coefficients corresponding to each failure mode, and the value of 1.0 or higher of them indicates that the corresponding failure criterion has been met.

Once the initial damage of materials appears, then the degradation of material properties would take place according to the damage evolution law. The evolution law for fiber damage was defined in the following equation (here $\alpha=1\pm, 2\pm$) [30],

$$d_{\alpha} = 1 - \frac{1}{r_{\alpha}} \exp \left[-\frac{2g_0^{\alpha} L_c}{G_{fc}^{\alpha} - g_0^{\alpha} L_c} (r_{\alpha} - 1) \right] \quad (11)$$

where L_c denotes the characteristic length of the element; G_{fc}^{α} is the fracture energy per unit area at the fiber tensile failure or fiber compressive failure; g_0^{α} is the elastic energy per unit volume under uniaxial tensile or compressive loading; r_{α} is the damage threshold for fiber damage and can be defined as (here $i= 1, 2$):

$$r_{i+} = \max(1, F_{i+}) \quad (12)$$

$$r_{i-} = \max(1, F_{i-}) \quad (13)$$

As for the shear damage evolution, it is assumed that d_{12} increases with logarithm of the damage threshold (r_{12}) until a specified maximum value was reached [30], and it was given by:

$$d_{12} = \min [\beta_{12} \ln(r_{12}), d_{12}^{max}] \quad (14)$$

where β_{12} and d_{12}^{max} are the material properties that can be determined experimentally. r_{α} is the damage threshold for shear and can be defined as:

$$r_{12} = \max(1, F_{12}) \quad (15)$$

The damage thresholds, r_{i+} , r_{i-} and r_{12} , reflect the historical damage of materials. They were initially set to 1 before the initial damage and equal to each corresponding failure coefficient when damage evolution occurs.

According to the experimental result shown in Fig. 3(b), it can be found that the in-plane shear response is dominated by the plastic behavior due to the matrix micro-cracking. To account for this plastic behavior, a plasticity model was implemented and the yield function

was given by:

$$F = |\hat{\sigma}_{12}| - \hat{\sigma}_0(\bar{\varepsilon}^{pl}) \leq 0 \quad (16)$$

and the hardening law was assumed to be of the form:

$$\hat{\sigma}_0(\bar{\varepsilon}^{pl}) = \hat{\sigma}_{y0} + C(\bar{\varepsilon}^{pl})^p \quad (17)$$

where $\hat{\sigma}_{y0}$ is the initial effective shear yield stress; C and p are the constants for the calibration of the hardening curve; $\bar{\varepsilon}^{pl}$ is the equivalent plastic strain. Note that the values of C , p , and $\hat{\sigma}_{y0}$ can be determined using a calibration procedure as presented in Ref. [30].

In order to develop the constitutive model for intra-laminar failure, the experimental results of the tensile test and the in-plane shear test (see Fig. 3) were completed with the material parameters reported in Ref. [30], where the similar materials were used. The values of elastic constants, damage initiation and fracture energies for a single ply along the fiber directions are presented in Table 2. The parameters describing the plastic deformation and failure behavior for a single ply under shear loading are summarized in Table 3.

Table 2 Material properties describing the elastic and failure behaviors along the fiber directions.

Table 3 Material properties describing the plastic deformation and failure behaviors under the shear loads.

3.1.2 Inter-laminar failure

The interface constitutive response was modeled using the cohesive contact method, which was defined based on the traction–separation law including corresponding damage criterion and evolution [30]. The inter-laminar behavior was considered to be linear elastic before the delamination occurred; and normal and shear traction components were assumed to be uncoupled within the elastic range. Therefore, the elastic behavior can be defined as:

$$\mathbf{t} = \begin{Bmatrix} t_n \\ t_s \\ t_t \end{Bmatrix} = \begin{bmatrix} K_n & 0 & 0 \\ 0 & K_s & 0 \\ 0 & 0 & K_t \end{bmatrix} \begin{Bmatrix} \varepsilon_n \\ \varepsilon_s \\ \varepsilon_t \end{Bmatrix} = \mathbf{K}\boldsymbol{\varepsilon} \quad (18)$$

where \mathbf{t} denotes traction stress vector and $\boldsymbol{\varepsilon}$ is the strain vector; subscripts n , s and t are the normal, first shear, and second shear directions, respectively; \mathbf{K} is the stiffness matrix of interaction.

To describe the initiation of delamination damage, a quadratic interaction function can be defined as [30]:

$$\left(\frac{t_n}{t_n^0}\right)^2 + \left(\frac{t_s}{t_s^0}\right)^2 + \left(\frac{t_t}{t_t^0}\right)^2 = 1 \quad (19)$$

where t_n^0 , t_s^0 and t_t^0 represent the peak values of the traction stresses. Once the function reaches a value of 1, the damage could take place and grow according to the damage evolution laws:

$$G_n^C + (G_s^C - G_n^C) \left(\frac{G_s + G_t}{G_n + G_s + G_t}\right)^\eta = G^C \quad (20)$$

where G is the fracture energy and superscript C represents the critical fracture energy; η is a cohesive property parameter. Table 4 presents the material properties to describe the inter-laminar damage model, and these parameters can be found in Ref. [30].

Table 4 Material properties describing the inter-laminar damage model.

3.2 The single shell layer model

The single shell layer model of the CFRP tube was implemented in commercial code ABAQUS, in which the material properties for defining the FE model are listed in Table 2 and Table 3. The single shell layer model for the tube without chamfer (T-1) is illustrated in Fig. 6, in which both the upper and the lower platens were modeled in the rigid surfaces. According to Eq. (11), the damage evolution law largely depends on the element size, which should be sufficiently small to keep d_a between 0 and 1. With consideration of the computational efficiency, the tube was meshed by the conventional shell elements (S4R) with a mesh size of 1.0×1.0 mm, which is sufficient to predict the crushing behaviors of the CFRP tube [30,37]. The constant velocity of 1 m/s was assigned to the moving upper platen, and the lower platen was fixed in all directions. Note that in the numerical simulation a much higher loading rate was used in order to balance computational efficiency and accuracy [38].

Fig. 6 The single shell model of the square CFRP tube without chamfer (T-1).

3.3 The stacked shell model

The stacked shell model of the specimen T-1 is shown in Fig. 7(a), where the two platens were modeled using the rigid surface. The detailed view as depicted in Fig. 7(b) indicates 9 layers, each representing one fiber ply of 0.22 mm in thickness; and each layer was meshed using continuum shell elements (SC8R) with a mesh size of 1.0×1.0 mm. This type of element has the geometry of the solid element, but the constitutive behaviors are similar to those of conventional shell elements [30]. The material properties defining the intra-laminar failure model are listed in Table 2 and Table 3. The cohesive contact model was used to simulate the delamination between the layers, and the material parameters to describe the cohesive contact are given in Table 4.

Fig. 7 (a) The stacked shell model of the specimen T-1; (b) The detail view of stacked-shell model.

4. Results and Discussion

In order to explore overall suitability of these two different modeling approaches, this section first depicts the effects of key modeling parameters by comparing with the experimental data of specimen T-1. Then, the suitable modeling approach is further validated by specimens T-2 and T-3.

4.1 Results of single layer model

This section discusses the simulation results of the single layer model for specimen T-1, through which the effect of key parameters on results are analyzed in detail. According to the literature [39], the frictional effect between fronds and platen can be observed during the crushing, which can be a significant contributor to the energy absorption. Therefore, three different values of friction coefficient μ (0.1, 0.15 and 0.2) were examined herein.

Figs. 8 and 9 show the force-displacement curves and deformation modes during the crushing process of T-1 with different coefficients (μ). The field variable is used to represent the damage of CFRP materials in the FE models, in which the red color indicates the failure elements (see Fig. 9). According to the deformation patterns shown in Fig. 9, all these three single layer models developed approximately the same deformation mode, in which progressive end-crushing mode together with local buckling mode were observed, indicating relatively little effect of friction coefficient on collapse modes. Compared with the

experimental results (see Fig. 5(a)), these three FE models were incapable of representing the delamination failure observed in the test, which implies the fundamental limitation of the single layer modeling approach. In other words, such models cannot realistically capture the failure mechanisms for energy absorption; thus these simulations significantly under-predicted the crushing load recorded from the tests, as shown in Fig. 8. In addition, it can be noted that the initial peak forces from the simulation are remarkably higher than that from the experimental test. This may be due to the fact that the delamination failure occurred in the experiment led to a relatively lower initial peak force.

Several crashworthiness indicators of T-1 calculated from the force-displacement curves are listed in Table 5. Note that increasing the friction coefficient from 0.1 to 0.2 enhances the energy absorption (*EA*), while the maximum *EA* value is still remarkably lower than the experimental counterpart. In general, it is evident that the simulation based on the single shell layer model was unable to capture the energy absorbing mechanisms properly and yielded considerable discrepancy with the testing results, specifically underestimating the crushing loads and *EA*.

Fig. 8 Force-displacement curves of the single shell layer models for T-1 with different μ .

Fig. 9 Deformation patterns of the single shell layer models for T-1 with different μ .

Table 5 Crashworthiness indicators of T-1 obtained from single shell layer models and the experimental test.

4.2 Results of stacked shell model

This section depicts the simulation results of T-1 obtained from the stacked shell modeling approach, and the effects of friction coefficient and the number of shell layers were discussed. Fig. 10 plots the force-displacement curves for the 9 layer stacked shell models (each shell layer represents one fiber ply) with three different friction coefficients ($\mu=0.1, 0.15, 0.2$) together with the test curve. Fig. 11 compares the deformation modes during the crushing process. It can be seen that increasing friction coefficient did not change the main collapse

mode. All the three configurations crushed in the same way; and the overall deformation modes in terms of delamination failure and fiber failure showed good agreement with those of the experimental test (see Fig. 5(a)). As shown in Fig. 10, increasing the friction coefficient from 0.1 to 0.2 slightly increased crushing load; and the trends of the predicted (e.g. $\mu = 0.2$) and tested curves are quite close. In view of these curves, it is worth noting that the predicted crushing loads are slightly higher than the experimental value in the later crushing stage. This may be due to the frictional effect in between the internal fronds and bottom platen. Further, the crashworthiness indicators calculated from the curves are listed in Table 6, which shows that EA raises slightly with increase in the friction coefficient. It can be concluded that the 9 layer stacked shell model with $\mu = 0.2$ is able to predict the crashworthiness indicators and simulate all complex failure modes of CFRP tube properly.

Fig. 10 Force-displacement curves of the stacked shell models with different μ .

Fig. 11 Deformation patterns of the stacked shell models with different μ .

Further, two other FE models, developed by different number (3 and 5) of shell layers in thickness, were also considered herein to explore the influence of number of shell layers. In these analyses, the friction coefficient was set to be 0.2 for all the models. Figs. 12 and 13 illustrate the force-displacement curves and deformation patterns of each tested configuration. It can be seen that a delamination failure mode did not occur in the 3 layer (each shell layer represents 3 fiber plies) and 5 layer (each shell layer represents 1.8 fiber plies) models, indicating that reducing the number of layers changed the mode of collapse. Additionally, the changes in deformation pattern led to an overestimated energy absorption, as shown in Table 6. As a result, it is shown that the 9 layer stacked shell model with $\mu = 0.2$ is capable of predicting the damage progression, failure modes and all the crashworthiness indicators of the specimen T-1 with relatively high accuracy.

Fig. 12 Force-displacement curves of the stacked shell models with different number of layers.

Fig. 13 Deformation patterns of the stacked shell models with different number of layers.

Table 6 Crashworthiness indicators obtained from the stacked shell FE models and the experimental test.

In order to further validate the modeling approach, the 9 layer stacked shell model ($\mu = 0.2$) is adopted to predict crushing behaviors of tubes with the chamfer (T-2 and T-3). Figs. 14 and 15 illustrated the simulation results of force-displacement curves and deformation modes for T-2 and T-3 respectively; and good agreement can be observed by comparing with the experimental results, further indicating a high accuracy of the stacked shell modeling approach.

Fig. 14 Force-displacement curves of the stacked shell models for T-2 and T-3: (a) T-2; (b) T-3.

Fig. 15 Deformation patterns of the stacked shell models for T-2 and T-3: (a) T-2; (b) T-3.

5. Comparison of crashworthiness between CFRP tubes with different sectional profiles

From the previous experimental and numerical analyses, 9 layer stacked shell model with $\mu = 0.2$ is able to provide sufficient accuracy for predicting the crushing behaviors of CFRP square tubes. Based on this modeling approach, this section further explores the crashworthiness characteristics of several other CFRP tubes with different sectional profiles, which helps select the best tubal profiles. These cross-sectional profiles under consideration include triangle, square, pentagon, hexagon and circle, as shown in Fig. 16. The perimeter of the cross section and the length of the tubes were made as constants (i.e. the same weight) for the purpose of comparison. The effects of tubal wall thickness on crashworthiness characteristics were explored. From the experimental results presented in section 2.5, it was known that there is little influence of chamfer on deformation mode and crashworthiness indicators of the tubes. Thus, the following investigation would not consider the chamfer.

Fig. 16 CFRP tubes with different sectional profiles: (a) Triangle; (b) Square; (c) Pentagon; (d) Hexagon; (e)

Circle.

5.1 Force–displacement curves and failure modes

The typical force–displacement curves and the crushing history for all these different sectional configurations with 9 fiber plies across the wall thickness were plotted in Fig. 17 and Fig. 18, respectively. It is noticeable that the overall trends of loading response and the values of PCF are fairly close to each other. Nevertheless, it is worth noting that the crushing load increases slightly with growing number of the edge; and the circular tube is of the highest load carrying capacity, as shown in Fig. 17. From the crushing history plotted in Fig. 18, it can be seen that progressive crushing of all tubes was developed with the propagation of the intra/interlaminar cracks which split the tubes into external and internal fronds. In addition, it can be also observed that with raising number of edges, the number of the axial cracks increased. Since the circular tube developed more cracks in the axial direction, it absorbed more energy, which explains why the circular tube has the highest crushing load and energy absorption capacity.

Fig. 17 Comparison of force–displacement curves between the different tubes with 9 fiber plies across the wall thickness.

Fig. 18 Comparison of deformation patterns between the different tubes with 9 fiber plies across the wall thickness.

In order to investigate the effect of tubal wall thickness on crashworthiness characteristics, the other two different wall thickness (7 fiber plies and 5 fiber plies) for all the configurations were also considered here. Figs. 19 and 20 plot the force–displacement curves and the crushing history for all the structures with 7 fiber plies across the wall thickness. In view of these curves, the crushing load of tubes with triangle, square and circle sections were seen a trend of gradual reduce towards the later stage of crushing process. This is due to the fact that the unstable local buckling mode (see Fig. 20(a), (b) and (e)) was observed in these tubes during the crushing, which led to a relatively low load carrying capacity. On the contrast, the progressive failure mode was observed in the tubes with pentagon and hexagon sections; and the crushing loads fluctuated around their means. Further, the deformation patterns of tubes with pentagon and hexagon sections were approximately the same as those of their 9 fiber plies counterparts. It can be concluded that there is a little effect of thickness when

changing from 9 fiber plies to 7 fiber plies on the deformation patterns for the tubes with pentagon and hexagon sections.

Fig. 19 Comparison of force-displacement curves between the different tubes with 7 fiber plies across the wall thickness.

Fig. 20 Comparison of deformation patterns between the different tubes with 7 fiber plies across the wall thickness.

Figs. 21 and 22 depict the force-displacement curves and some snapshots of deformation modes for all the tubes with 5 fiber plies across the wall thickness. With increasing crushing displacement, it can be seen that the crushing loads for all the configurations showed a trend of decrease at different levels. This is mainly because that the excessive reduction in tubal wall thickness led to the changes in deformation patterns; and unstable local buckling mode can be observed in all the tubes, as shown in Fig. 22. As a result, it can be concluded that the reduction in the wall thickness from 7 fiber plies to 5 fiber plies led to noticeable changes in deformation patterns for all the configurations, and thereby considerably reducing the crushing loads.

Fig. 21 Comparison of force-displacement curves between the different tubes with 5 fiber plies across the wall thickness.

Fig. 22 Comparison of deformation patterns between the different tubes with 5 fiber plies across the wall thickness.

5.2 Comparison of energy absorption characteristics

The crashworthiness indicators were derived from the force-displacement curves to investigate crashworthiness characteristics of all these configurations, as presented in Table 7.

Fig. 23 shows the bar chart of *SEA* for all the tubes with different thicknesses. It can be seen that the effect of wall thickness on *SEA* of tubes with the pentagon, hexagon and circle profiles is relatively small compared with the triangle and square profiles. The value of *SEA* for hexagon tube reached the maximum value at the 7 fiber plies across the wall thickness. For the tubes with the same wall thickness, the values of *SEA* increased with raising the number of edges. Therefore, the circle tube shows superior specific energy absorption

capacity over all the other tubes with the same wall thickness, indicating that the circular CFRP tube section is of good potential as a crashworthy structure.

Table 7 Crashworthiness indicators for all configurations.

Fig. 23 *SEA* of all configurations.

6. Conclusions

This study developed two different numerical models (namely single layer shell model and stacked shell model) based on a proposed constitutive model to simulate experimental crush tests on a square CFRP tube. The influence of key modeling parameters for these two FE models were analyzed; and their overall suitability was assessed to provide an effective and accurate prediction. Further, the crushing behaviors of several CFRP tubes with different cross sectional shapes and wall thickness have been investigated through numerical simulations to explore the most suitable sectional configurations for crashworthiness design. Within the limitations, the following conclusion can be drawn from this study:

(1) The simulation based on the single shell layer model is unable to realistically capture the failure mechanism and energy absorption capacity obtained from the experimental tests, specifically underestimating the crushing loads and *EA* considerably.

(2) The 9 layer stacked model with $\mu = 0.2$ is able to predict the damage progression, failure modes and the crashworthiness indicators of the CFRP square tube most accurately in comparison of the experimental results.

(3) Raising the friction coefficient increases the *EA* for both the FE models.

(4) In the stacked shell model, reducing the number of layers may change the main collapse mode, and consequently vary the value of *EA*.

(5) For the tubes with different sectional profiles but the same wall thickness and perimeter (this the same weight), the *SEA* increases with raising the number of edges. The effect of thickness on *SEA* of tubes with pentagon, hexagon and circle profiles is relatively small in comparison with the triangle and square profiles. The circular tube exhibits superior energy absorption capacity of all these tubes concerned, thereby being of great potential to be

a crashworthy structure.

Acknowledgements

This work is supported by National Natural Science Foundation of China (51575172). Dr. Sun is a recipient of Australian Research Council (ARC) DECRA Fellow (DE160101633).

References

- [1] McCarthy RFJ, Haines GH, Newley RA. Polymer composite applications to aerospace equipment. *Composites Manufacturing* 1994; 5(2):83-93.
- [2] Beardmore P, Johnson CF. The potential for composites in structural automotive applications. *Composites Science & Technology* 1986; 26(4):251-281.
- [3] Vaidya UK. Design and manufacture of woven reinforced glass/polypropylene composites for mass transit floor structure. *Journal of Composite Materials* 2004; 38(21):1949-1971.
- [4] Ning H, Pillay S, Vaidya U K. Design and development of thermoplastic composite roof door for mass transit bus. *Materials & Design*, 2009, 30(4):983-991.
- [5] Bartus S D, Vaidya UK, Ulven CA. Design and development of a long fiber thermoplastic bus seat. *Journal of Thermoplastic Composite Materials* 2006; 19(2):131-154.
- [6] Hussein RD, Ruan D, Lu G, Sbarski I. Axial crushing behaviour of honeycomb-filled square carbon fibre reinforced plastic (CFRP) tubes. *Composite structures* 2016; 140: 166-179.
- [7] Joosten MW, Dutton S, Kelly D, Thomson R. Experimental and numerical investigation of the crushing response of an open section composite energy absorbing element. *Composite Structures* 2011; 93(2): 682-689.
- [8] Feraboli P, Wade B, Deleo F, Rassaian M, Higgins M. LS-DYNA MAT54 modeling of the axial crushing of a composite tape sinusoidal specimen. *Composites Part A: Applied Science and Manufacturing* 2011; 42(11): 1809-1825.
- [9] Liu Q, Lin Y, Zong Z, Sun G, Li Q. Lightweight design of carbon twill weave fabric composite body structure for electric vehicle. *Composite Structures* 2013; 97: 231-238.
- [10] Park CK, Kan CD, Hollowell WT. Evaluation of crashworthiness of a carbon-fiber-reinforced polymer (CFRP) ladder frame in a body-on-frame vehicle. *International Journal of Crashworthiness* 2014; 19(1): 27-41.
- [11] Feraboli P, Masini A, Taraborrelli L, Pivetti A. Integrated development of CFRP structures for a topless high performance vehicle. *Composite Structures* 2007; 78(4): 495-506.
- [12] Feraboli P, Masini A. Development of carbon/epoxy structural components for a high performance vehicle. *Composites Part B Engineering* 2004; 35(4):323-330.
- [13] Kang KT, Chun HJ, Park JC, Na WJ, Hong HT, Hwang IH. Design of a composite roll bar for the improvement of bus rollover crashworthiness. *Composites Part B Engineering* 2012; 43(4):1705-13.
- [14] Obradovic J, Boria S, Belingardi G. Lightweight design and crash analysis of composite frontal impact

- energy absorbing structures. *Composite Structures* 2012; 94(2): 423-430.
- [15] Mahdi E, Hamouda AMS, Sebaey TA. The effect of fiber orientation on the energy absorption capability of axially crushed composite tubes. *Materials & Design* 2014; 56(4):923-928.
- [16] Israr HA, Rivallant S, Barrau JJ. Experimental investigation on mean crushing stress characterization of carbon–epoxy plies under compressive crushing mode. *Composite Structures* 2013; 96(4):357-364.
- [17] Zhu G, Li S, Sun G, Li G, Li Q. On design of graded honeycomb filler and tubal wall thickness for multiple load cases. *Thin-Walled Structures* 2016; 109:377-389.
- [18] Nia AA, Parsapour M. Comparative analysis of energy absorption capacity of simple and multi-cell thin-walled tubes with triangular, square, hexagonal and octagonal sections. *Thin-Walled Structures* 2014; 74: 155-165.
- [19] Tarlochan F, Samer F, Hamouda AMS, Ramesh S, Khalid K. Design of thin wall structures for energy absorption applications: enhancement of crashworthiness due to axial and oblique impact forces. *Thin-Walled Structures* 2013; 71: 7-17.
- [20] Zhang Y, Lu M, Sun G, Li G, Li Q. On functionally graded composite structures for crashworthiness. *Composite Structures* 2015; 132: 393-405.
- [21] Sun G, Tian X, Fang J, Xu F, Li G. Dynamical bending analysis and optimization design for functionally graded thickness (FGT) tube. *International Journal of Impact Engineering* 2015; 78: 128-137.
- [22] Greco F, Luciano R. A theoretical and numerical stability analysis for composite micro-structures by using homogenization theory. *Composites Part B Engineering* 2011; 42(3):382-401.
- [23] Sun H, Di S, Zhang N, Pan N, Wu C. Micromechanics of braided composites via multivariable FEM. *Computers & Structures* 2003; 81(20):2021-2027.
- [24] Tabiei A, Aminjikai SB. A strain-rate dependent micro-mechanical model with progressive post-failure behavior for predicting impact response of unidirectional composite laminates. *Composite Structures* 2009; 88(1):65-82.
- [25] Chiu LNS, Falzon BG, Boman R, Chen B, Yan W. Finite element modelling of composite structures under crushing load. *Composite Structures* 2015; 131:215-228.
- [26] Liu Z, Lu J, Zhu P. Lightweight design of automotive composite bumper system using modified particle swarm optimizer. *Composite Structures* 2016; 140:630-643.
- [27] Luo H, Yan Y, Meng X, Jin C. Progressive failure analysis and energy-absorbing experiment of composite tubes under axial dynamic impact. *Composites Part B: Engineering* 2016; 87:1-11.
- [28] Boria S, Obradovic J, Belingardi G. Experimental and numerical investigations of the impact behaviour of composite frontal crash structures. *Composites Part B: Engineering* 2015; 79: 20-27.
- [29] Bussadori BP, Schuffenhauer K, Scattina A. Modelling of CFRP crushing structures in explicit crash analysis. *Composites Part B Engineering* 2014; 60(1):725-735.

- [30] Sokolinsky VS, Indermuehle KC, Hurtado JA. Numerical simulation of the crushing process of a corrugated composite plate. *Composites Part A: Applied Science and Manufacturing* 2011; 42(9): 1119-1126.
- [31] Xiao X, Botkin ME, Johnson NL. Axial crush simulation of braided carbon tubes using MAT58 in LS-DYNA. *Thin-Walled Structures* 2009; 47(6): 740-749.
- [32] Fang J, Sun G, Qiu N, Kim NH, Li Q. On design optimization for structural crashworthiness and its state of the art. *Structural & Multidisciplinary Optimization* 2017; 55(3):1-29.
- [33] Sun G, Pang T, Fang J, Li G, Li Q. Parameterization of criss-cross configurations for multiobjective crashworthiness optimization. *International Journal of Mechanical Sciences* 2017; 124-125:145-157.
- [34] Liu Q, Xing H, Ju Y, Ou Z, Li Q. Quasi-static axial crushing and transverse bending of double hat shaped CFRP tubes. *Composite Structures* 2014; 117(1):1-11.
- [35] Wu W, Liu Q, Zong Z, Sun G, Li Q. Experimental investigation into transverse crashworthiness of CFRP adhesively bonded joints in vehicle structure. *Composite Structures* 2013; 106(12):581-589.
- [36] Liu Q, Ma J, Xu X, Wu Y, Li Q. Load bearing and failure characteristics of perforated square CFRP tubes under axial crushing. *Composite Structures* 2017; 160:23-35.
- [37] Esnaola A, Elguezal B, Aurrekoetxea J, Gallego I, Ulacia I. Optimization of the semi-hexagonal geometry of a composite crush structure by finite element analysis. *Composites Part B Engineering* 2016; 93:56-66.
- [38] Mamalis AG, Manolacos DE, Ioannidis MB, Papapostolou DP. The static and dynamic axial collapse of CFRP square tubes: finite element modeling. *Composite structures* 2006; 74(2): 213-225.
- [39] Mamalis AG, Manolacos DE, Ioannidis MB, Papapostolou DP. On the response of thin-walled CFRP composite tubular components subjected to static and dynamic axial compressive loading: experimental. *Composite Structures* 2005; 69(4):407-420.

Figure Captions

- Fig. 1** (a) The CFRP tube without chamfer (T-1); (b) The CFRP tube with single-sided chamfer (T-2); (c) The CFRP tube with bar chamfer (T-3).
- Fig. 2** Specimens for tensile tests and shear test: (a) The specimen and fiber orientations for tensile test; (b) The specimen and fiber orientations for shear test; (c) The specimen with CFRP tabs and speckle for DIC; (d) The specimen in the testing machine and set-up of DIC system.
- Fig. 3** Typical stress–strain curves of CFRP materials: (a) Tensile tests; (b) Shear tests.
- Fig. 4** (a) Typical force–displacement curves; (b) Crushing history of the CFRP tubes in axial crushing tests.
- Fig. 5** All specimens after compressive test: (a) T-1; (b) T-2; (c) T-3.
- Fig. 6** The single shell model of the square CFRP tube.
- Fig. 7** (a) The stacked shell model of the CFRP tube; (b) The detail view of stacked-shell model.
- Fig. 8** Force-displacement curves of the single shell layer models for T-1 with different μ .
- Fig. 9** Deformation patterns of the single shell layer models for T-1 with different μ .
- Fig. 10** Force-displacement curves of the stacked shell models for T-1 with different μ .
- Fig. 11** Deformation patterns of the stacked shell models for T-1 with different μ .
- Fig. 12** Force-displacement curves of the stacked shell models for T-1 with different number of layers.
- Fig. 13** Deformation patterns of the stacked shell models for T-1 with different number of layers.
- Fig. 14** Force-displacement curves of the stacked shell models for T-2 and T-3: (a) T-2; (b) T-3.
- Fig. 15** Deformation patterns of the stacked shell models for T-2 and T-3: (a) T-2; (b) T-3.
- Fig. 16** CFRP tubes with different sectional profiles: (a) Triangle; (b) Square; (c) Pentagon; (d) Hexagon; (e) Circle.
- Fig. 17** Comparison of force–displacement curves between the different tubes with 9 fiber plies across the wall thickness.
- Fig. 18** Comparison of deformation patterns between the different tubes with 9 fiber plies across the wall thickness.
- Fig. 19** Comparison of force-displacement curves between the different tubes with 7 fiber plies across the wall thickness.
- Fig. 20** Comparison of deformation patterns between the different tubes with 7 fiber plies across the wall thickness.

Fig. 21 Comparison of force–displacement curves between the different tubes with 5 fiber plies across the wall thickness.

Fig. 22 Comparison of deformation patterns between the different tubes with 5 fiber plies across the wall thickness.

Fig. 23 *SEA* of all configurations.

ACCEPTED MANUSCRIPT

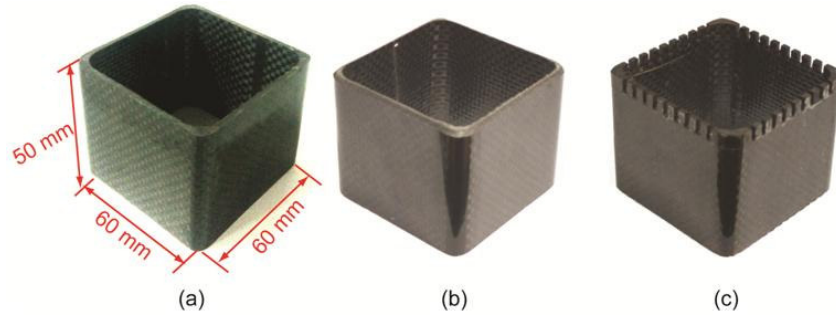


Fig. 1 (a) The CFRP tube without chamfer (T-1); (b) The CFRP tube with single-sided chamfer (T-2); (c) The CFRP tube with bar chamfer (T-3).

ACCEPTED MANUSCRIPT

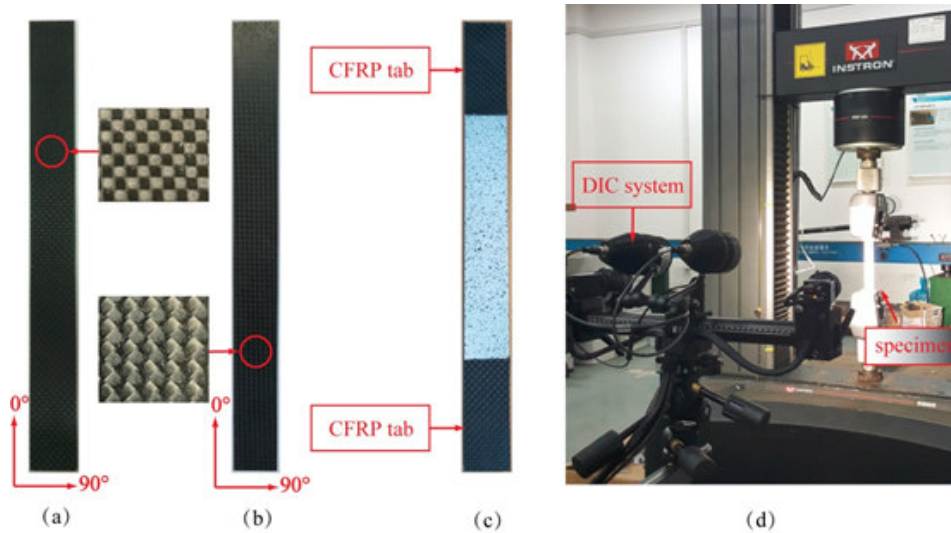


Fig. 2 Specimens for tensile tests and shear test: (a) The specimen and fiber orientations for tensile test; (b) The specimen and fiber orientations for shear test; (c) The specimen with CFRP tabs and speckle for DIC; (d) The specimen in the testing machine and set-up of DIC system.

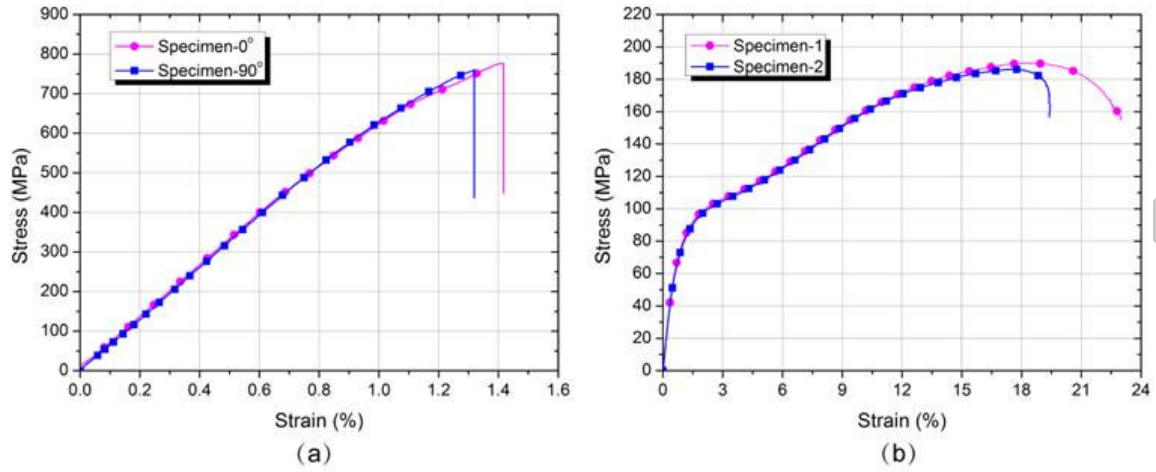


Fig. 3 Typical stress–strain curves of CFRP materials: (a) Tensile tests; (b) Shear tests.

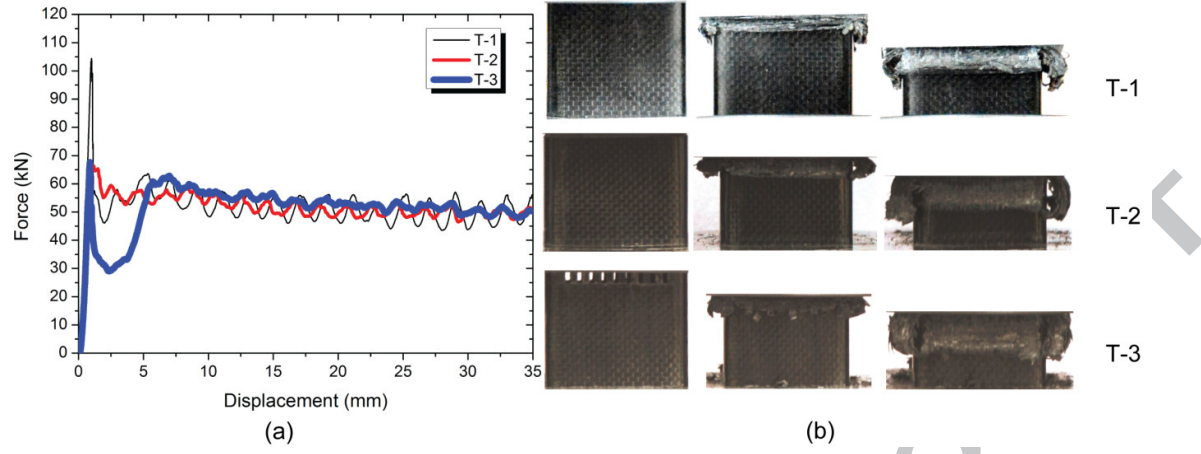


Fig. 4 (a) Typical force–displacement curves; (b) Crushing history of the CFRP tubes in axial crushing tests.

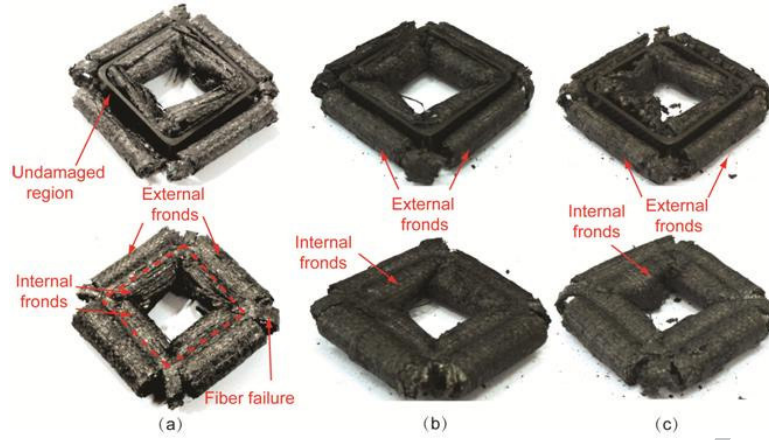


Fig. 5 All specimens after compressive test: (a) T-1; (b) T-2; (c) T-3.

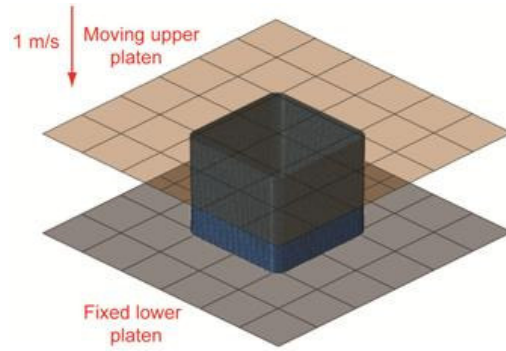


Fig. 6 The single shell model of the square CFRP tube.

ACCEPTED MANUSCRIPT

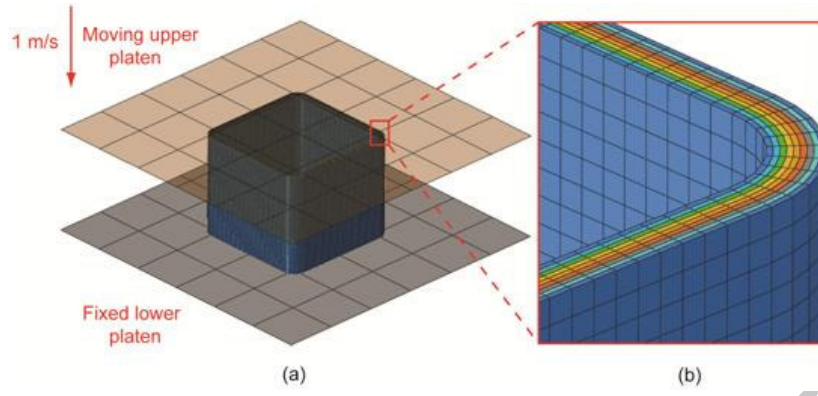


Fig. 7 (a) The stacked shell model of the CFRP tube; (b) The detail view of stacked-shell model.

ACCEPTED MANUSCRIPT

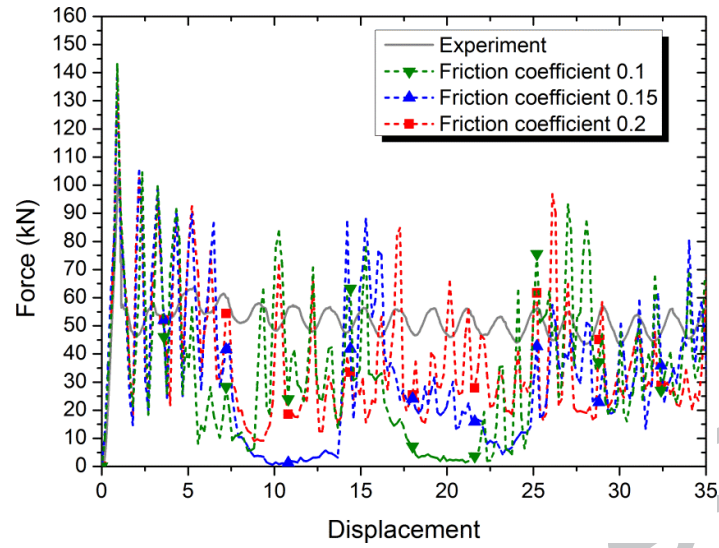


Fig. 8 Force-displacement curves of the single shell layer models for T-1 with different μ .

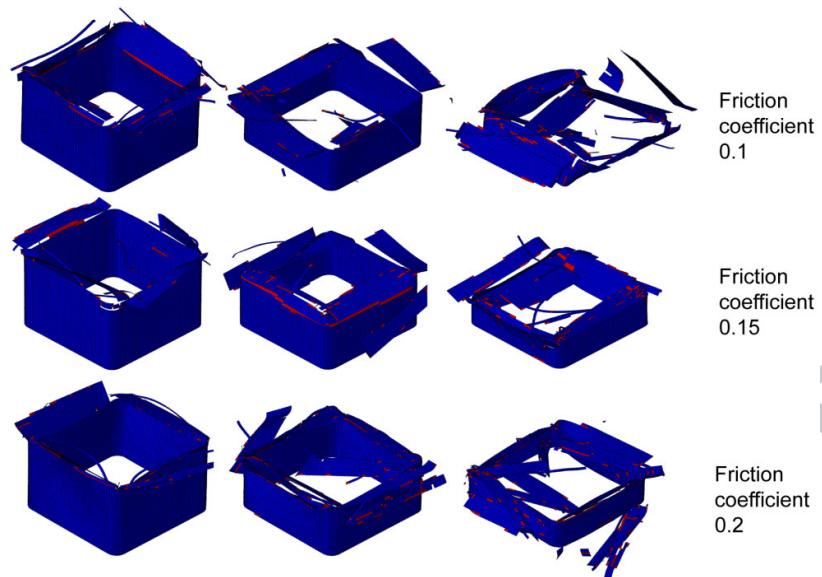


Fig. 9 Deformation patterns of the single shell layer models for T-1 with different μ .

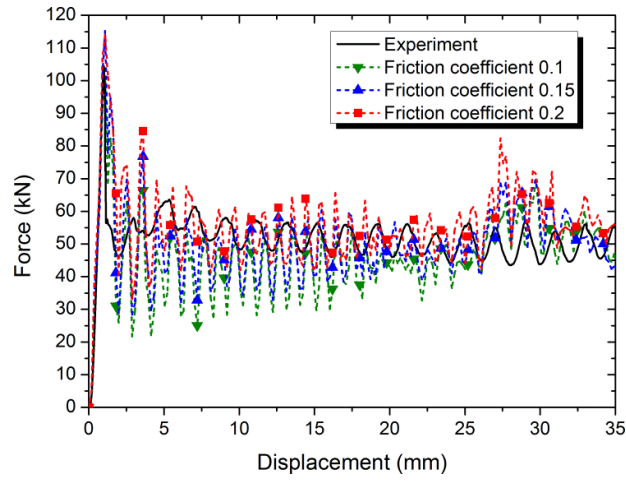


Fig. 10 Force-displacement curves of the stacked shell models for T-1 with different μ .

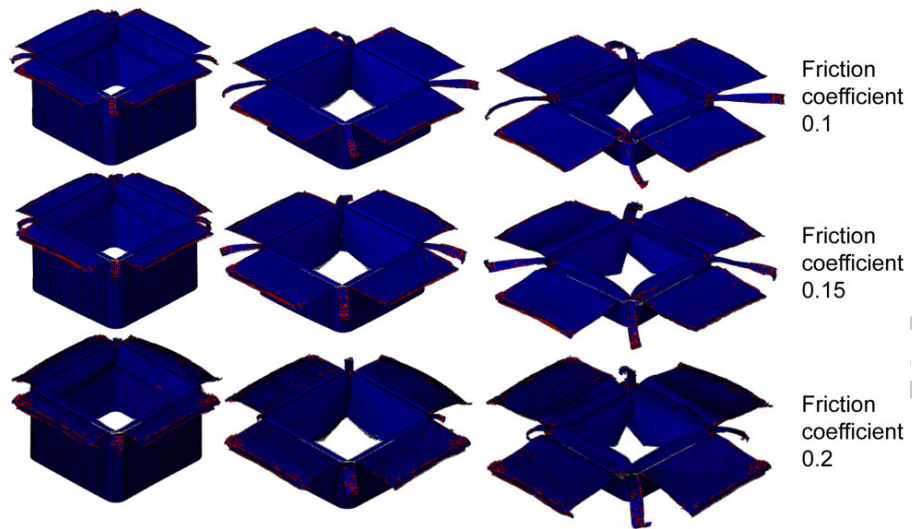


Fig. 11 Deformation patterns of the stacked shell models for T-1 with different μ .

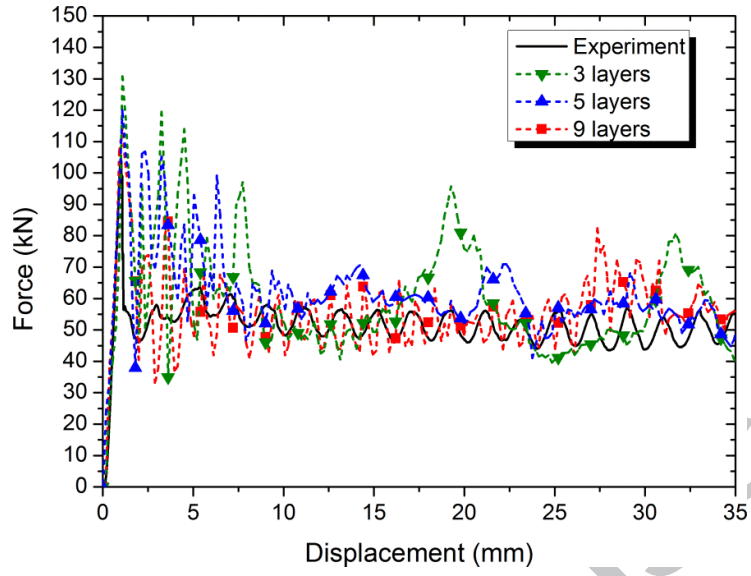


Fig. 12 Force-displacement curves of the stacked shell models for T-1 with different number of layers.

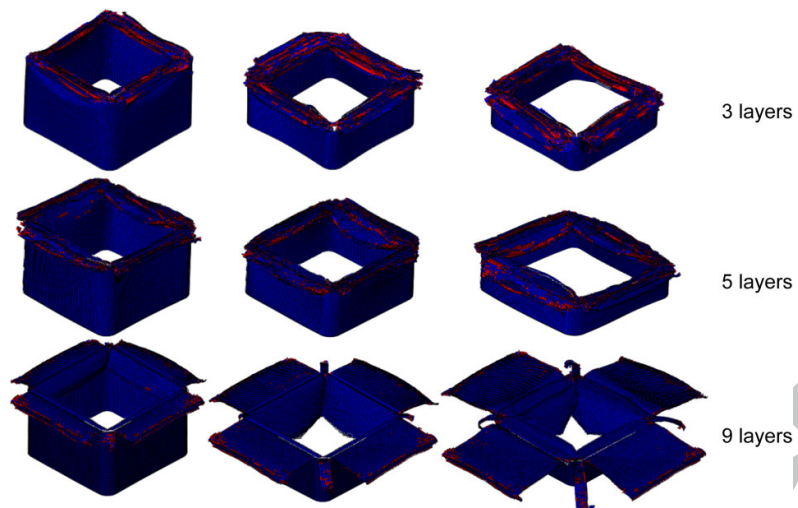


Fig. 13 Deformation patterns of the stacked shell models for T-1 with different number of layers.

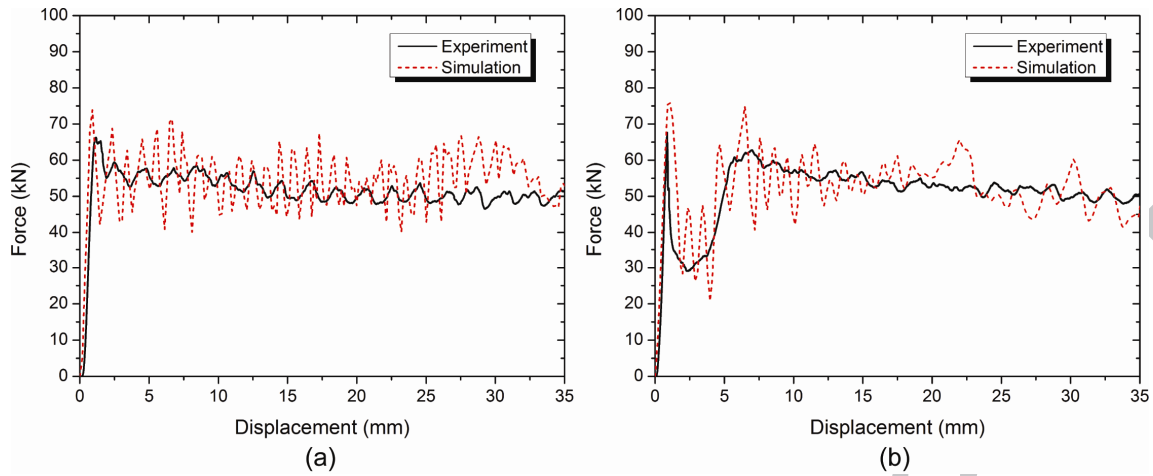


Fig. 14 Force-displacement curves of the stacked shell models for T-2 and T-3: (a) T-2; (b) T-3.

ACCEPTED MANUSCRIPT

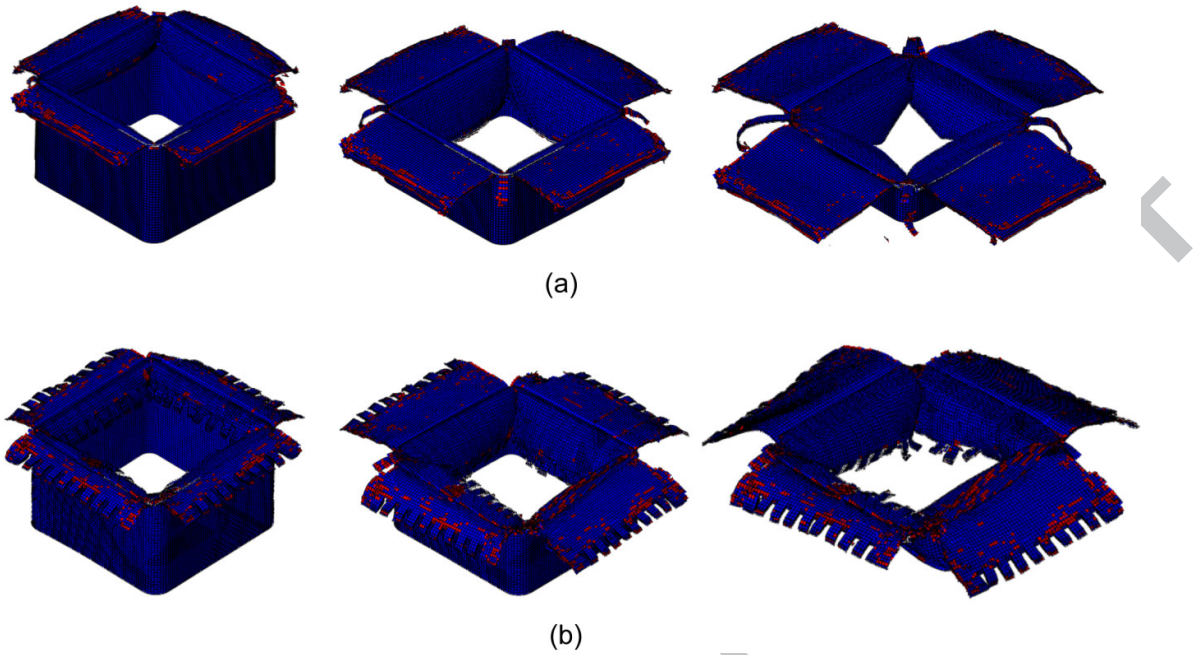


Fig. 15 Deformation patterns of the stacked shell models for T-2 and T-3: (a) T-2; (b) T-3.

ACCEPTED MANUSCRIPT

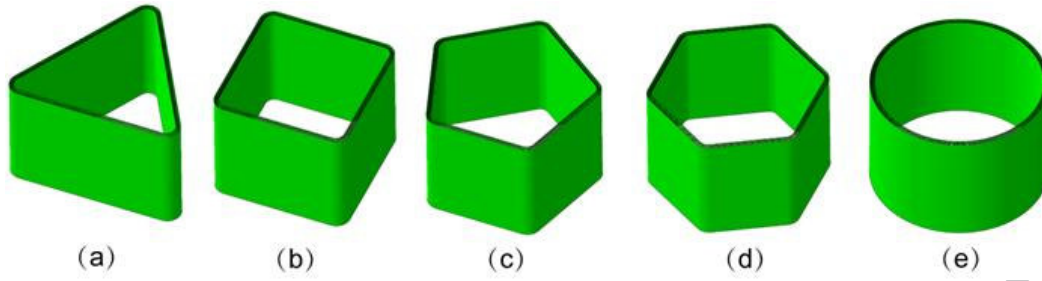


Fig. 16 CFRP tubes with different sectional profiles: (a) Triangle; (b) Square; (c) Pentagon; (d) Hexagon; (e) Circle.

ACCEPTED MANUSCRIPT

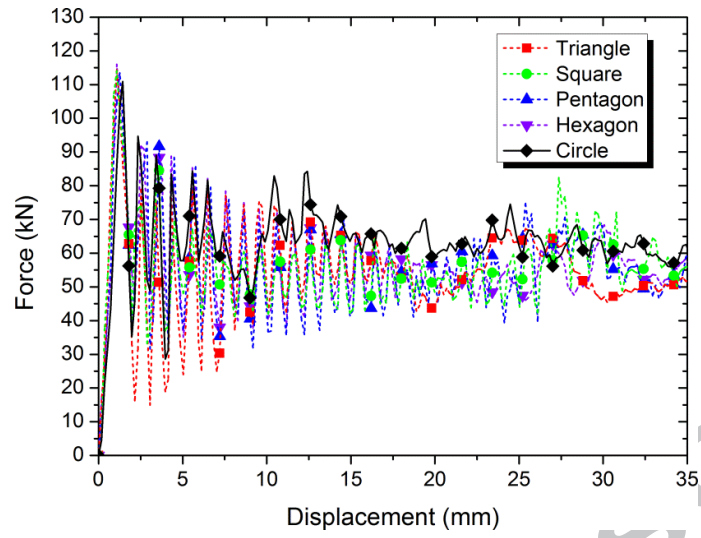


Fig. 17 Comparison of force–displacement curves between the different tubes with 9 fiber plies across the wall thickness.

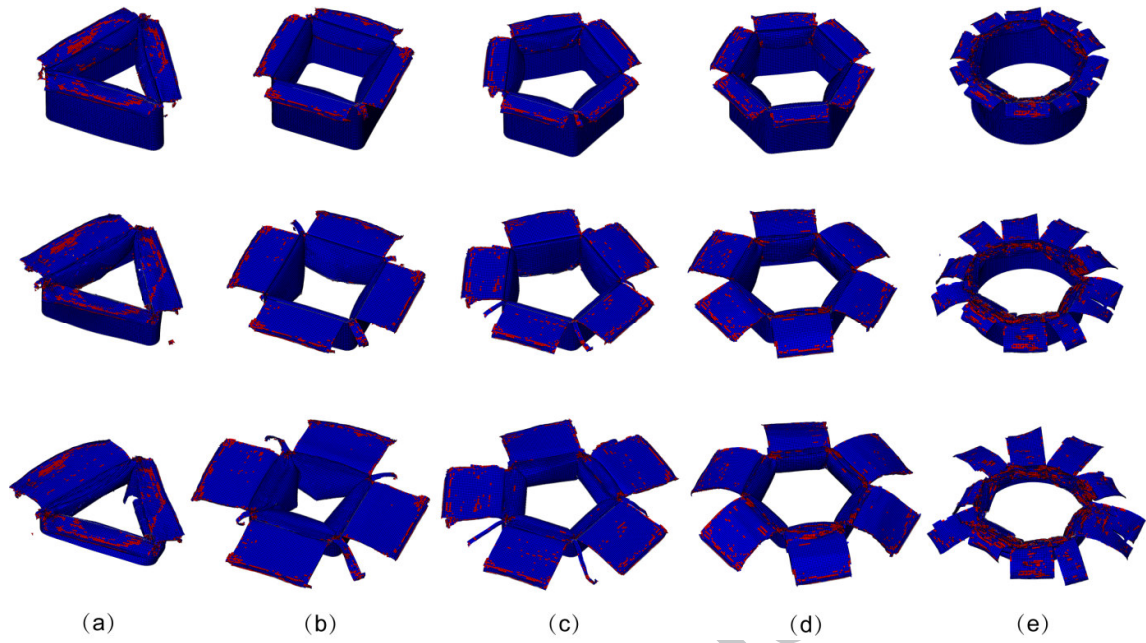


Fig. 18 Comparison of deformation patterns between the different tubes with 9 fiber plies across the wall thickness.

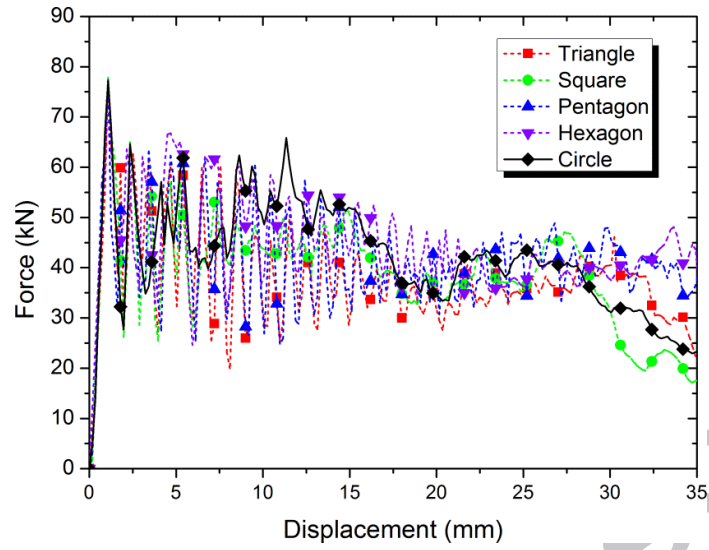


Fig. 19 Comparison of force-displacement curves between the different tubes with 7 fiber plies across the wall thickness.

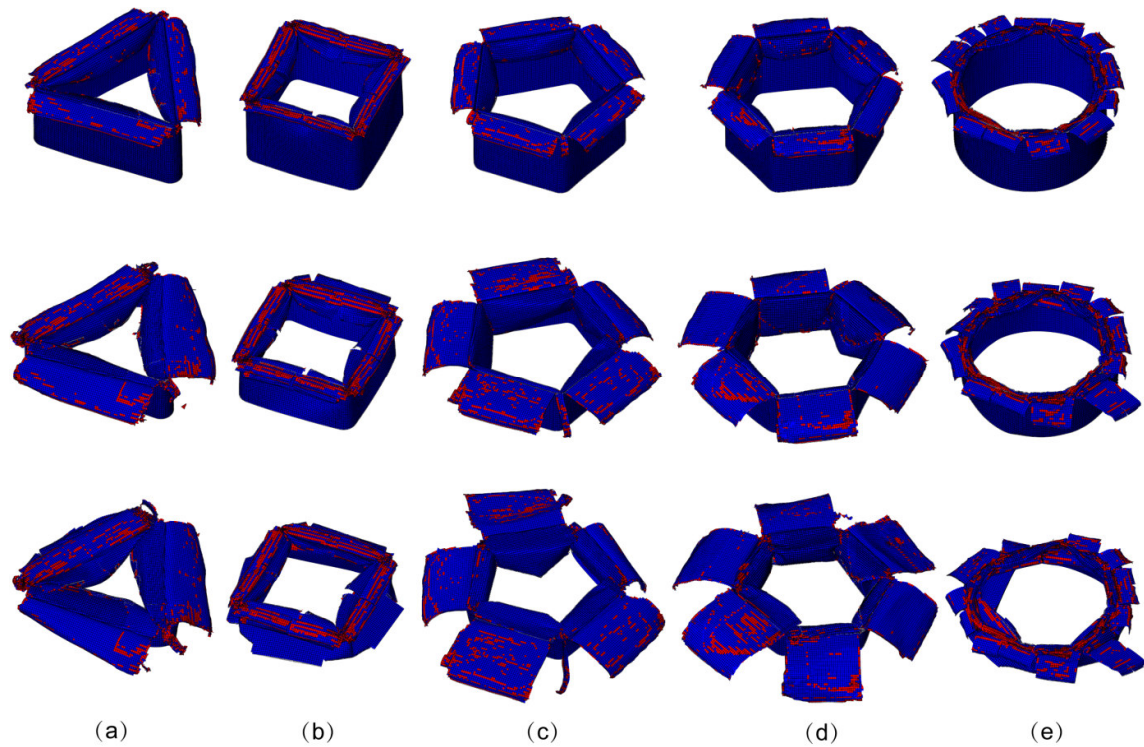


Fig. 20 Comparison of deformation patterns between the different tubes with 7 fiber plies across the wall thickness.

ACCEPTED MANUSCRIPT

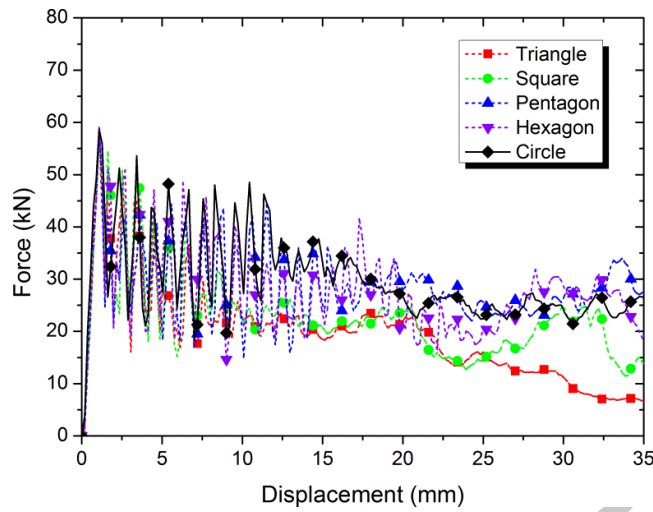


Fig. 21 Comparison of force–displacement curves between the different tubes with 5 fiber plies across the wall thickness.

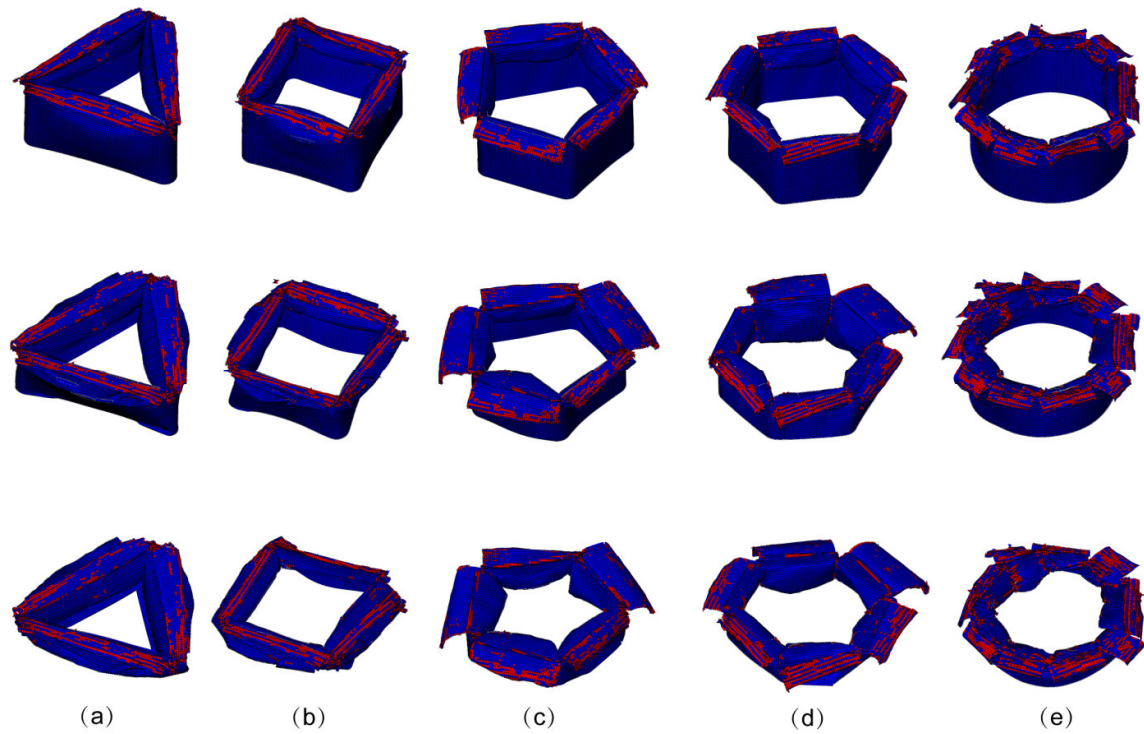


Fig. 22 Comparison of deformation patterns between the different tubes with 5 fiber plies across the wall thickness.

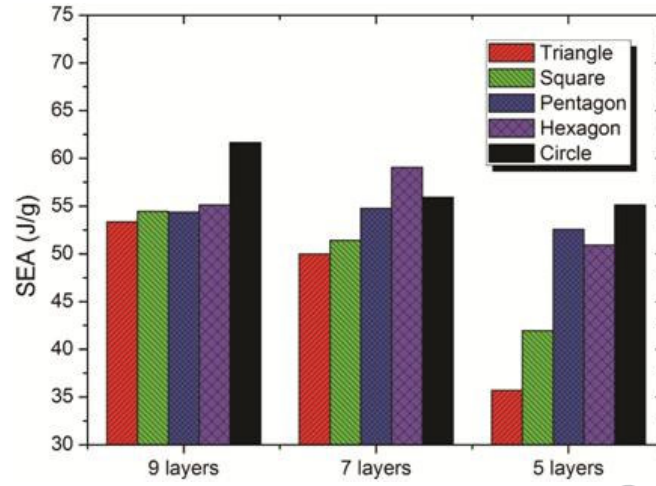


Fig. 23 SEA of all configurations.

Table Titles

Table 1 Crashworthiness indicators obtained from the crushing experimental tests.

Table 2 Material properties describing the elastic and failure behaviors along the fiber directions.

Table 3 Material properties describing the plastic deformation and failure behaviors under the shear loads.

Table 4 Material properties describing the inter-laminar damage model.

Table 5 Crashworthiness indicators of T-1 obtained from single shell layer models and the experimental test.

Table 6 Crashworthiness indicators obtained from the stacked shell FE models and the experimental test.

Table 7 Crashworthiness indicators for all configurations.

ACCEPTED MANUSCRIPT

Table 1 Crashworthiness indicators obtained from the crushing experimental tests.

Specimens	EA (J)	F_{mean} (kN)	PFC (kN)	CFE	SEA (J/g)
T-1	1808.93	52.38	104.38	0.50	50.25
T-2	1796.93	51.14	66.22	0.77	50.61
T-3	1778.35	50.82	67.72	0.76	51.10

ACCEPTED MANUSCRIPT

Table 2 Material properties describing the elastic and failure behaviors along the fiber directions.

Description	Variable	Value
Density (kg/m ³)	ρ	1560
Elastic properties (GPa)	E_1	65.1
	E_2	64.4
	G_{12}	4.5
	ν_{12}	0.037
Damage initiation (MPa)	X_{1+}	776
	X_{1-}	704
	X_{2+}	760
	X_{2-}	698
	S	95
Fracture energies (kJ/m ²)	G_{fc}^{1+}	125
	G_{fc}^{1-}	250
	G_{fc}^{2+}	95
	G_{fc}^{2-}	245

Table 3 Material properties describing the plastic deformation and failure behaviors under the shear loads.

Description	Variable	Value
Coefficient in the shear damage variable (Eq. (14))	β_{12}	0.18
Maximum value of shear damage variable	d_{12}^{max}	0.99
Initial effective shear yield stress (MPa)	$\hat{\sigma}_{y0}$	185
Power term in the hardening equation (Eq. (17))	p	0.41
Coefficient in the hardening equation (Eq. (17))	C	1053

ACCEPTED MANUSCRIPT

Table 4 Material properties describing the inter-laminar damage model.

Description	Variable	Value
Damage initiation (MPa)	t_n^0	54
	t_s^0	70
	t_t^0	70
Fracture energies (J/m ²)	G_n^C	504
	G_s^C	1566
	G_t^C	1566
BK	η	2.284

Table 5 Crashworthiness indicators of T-1 obtained from single shell layer models and the experimental test.

Type	EA (J)	F_{mean} (kN)	PCF (kN)	CFE	SEA (J/g)
Experimental test	1808.93	52.38	104.38	0.50	50.25
model with $\mu = 0.1$	1192.66	33.78	143.07	0.24	33.13
model with $\mu = 0.15$	1137.66	32.43	142.33	0.23	31.60
model with $\mu = 0.2$	1307.90	37.39	142.01	0.26	36.33

ACCEPTED MANUSCRIPT

Table 6 Crashworthiness indicators obtained from the stacked shell FE models and the experimental test.

Type	EA (J)	F_{mean} (kN)	PFC (kN)	CFE	SEA (J/g)
Experimental test	1808.93	52.38	104.38	0.50	50.25
9 layers model with $\mu = 0.1$	1622.53	46.04	100.17	0.46	40.07
9 layers model with $\mu = 0.15$	1759.34	49.88	115.24	0.43	48.87
9 layers model with $\mu = 0.2$	1960.19	55.62	114.12	0.49	54.45
3 layers model with $\mu = 0.2$	2101.74	59.53	130.82	0.46	58.38
5 layers model with $\mu = 0.2$	2085.14	58.34	120.09	0.49	57.92

ACCEPTED MANUSCRIPT

Table 7 Crashworthiness indicators for all configurations.

Type	Fiber plies	EA (J)	F_{mean} (kN)	PFC (kN)	CFE	SEA (J/g)
Triangle section	9	1920.49	54.49	114.47	0.48	53.35
Square section	9	1960.19	55.62	114.12	0.49	54.45
Pentagon section	9	1957.11	54.44	113.51	0.48	54.36
Hexagon section	9	1984.42	56.24	116.06	0.48	55.12
Circle section	9	2219.93	63.07	110.91	0.57	61.66
Triangle section	7	1325.12	37.49	77.49	0.48	50.00
Square section	7	1362.46	38.57	77.86	0.50	51.41
Pentagon section	7	1451.27	41.14	77.43	0.53	54.76
Hexagon section	7	1565.26	44.38	77.06	0.58	59.07
Circle section	7	1482.24	42.00	77.16	0.54	55.93
Triangle section	5	681.99	19.28	58.19	0.33	35.71
Square section	5	800.99	22.70	57.50	0.39	41.94
Pentagon section	5	1003.94	28.46	58.05	0.49	52.56
Hexagon section	5	972.54	27.59	59.08	0.47	50.92
Circle section	5	1053.06	29.89	58.66	0.51	55.13